

# Direct Numerical Simulation of Supersonic Film Cooling by Tangential Blowing



Johannes M. F. Peter and Markus J. Kloker

**Abstract** Film cooling is an effective method to thermally protect the nozzle extension of rocket engines from the hot exhaust gases. A cool secondary gas is blown into the supersonic hot-gas turbulent boundary layer through a backward-facing step to generate a cooling film that reduces the heat load of the structure. In this work the complex interaction between the hot supersonic main-flow and the coolant stream is investigated using high-order direct numerical simulations (DNS) to gain fundamental understanding of the mixing physics. The cooling gas is injected at a Mach number of 1.8 into the turbulent Mach-3.3 flat-plate boundary-layer at zero pressure gradient. The main gas is steam (gaseous  $\text{H}_2\text{O}$ ), the cooling gas is helium, and adiabatic wall conditions are used. Results for various blowing ratios  $F$  at kept cooling-gas temperature and Mach number are presented. The interaction of the main stream turbulence and the initially laminar cooling film is investigated in detail as well as the evolution of the cooling effectiveness. The common Goldstein correlation formula for the effectiveness is applied, but no satisfying scaling is achieved.

## 1 Introduction

The structure of modern, high-thrust rocket engines with their high chamber pressure and temperatures is subject to extreme thermal loads. Without active cooling, the wall temperatures would far exceed the limits of today's available materials. Hence, innovative and efficient cooling strategies have to be developed. An effective method also for the nozzle-extension is film cooling, where a cool secondary gas is blown into the hot supersonic main-flow boundary layer near the wall to generate a cooling film that reduces the heat load of the structure near and possibly downstream of the injection location. Beneficial coolant properties are a high heat capacity and

---

J. M. F. Peter (✉) · M. J. Kloker  
Institute of Aerodynamics and Gas Dynamics, University of Stuttgart,  
Pfaffenwaldring 21, 70569 Stuttgart, Germany  
e-mail: [peter@iag.uni-stuttgart.de](mailto:peter@iag.uni-stuttgart.de)

M. J. Kloker  
e-mail: [kloker@iag.uni-stuttgart.de](mailto:kloker@iag.uni-stuttgart.de)

© Springer Nature Switzerland AG 2021  
W. E. Nagel et al. (eds.), *High Performance Computing in Science and Engineering '19*,  
[https://doi.org/10.1007/978-3-030-66792-4\\_18](https://doi.org/10.1007/978-3-030-66792-4_18)

low thermal conductivity. The cooling gas can be injected either by wall-normal blowing through holes or slits (see, e.g., [12, 18]) or in wall-parallel fashion by blowing through a backward-facing step (see, e.g., [9, 11, 16]). The cooling efficiency depends on various parameters such as cooling-gas type and temperature, mass flux, and the mixing-flow characteristics. In this work, the complex interaction between the turbulent main and the coolant flow is investigated using high-order direct numerical simulation (DNS). The aim is to identify the fundamental parameters and physical phenomena governing the unavoidable mixing process and the subsequent decrease of the cooling effect downstream of the injection. Further research goals are to examine existing film-cooling correlations, to provide design-guidelines for film-cooling applications and reference cases for turbulence modelling used in faster simulations tools like RANS or LES. The DNS are performed for the introduction of a laminar, cold coolant stream into a turbulent, hot boundary-layer flow at formally zero streamwise pressure gradient. The principal flow setup is based on experimental investigations performed by sub-project A2 [19] of the German Collaborative Research Center SFB-TRR40 (in a nozzle extension). The main features of the flow have been approximately analyzed using RANS, and the DNS are now performed for a subdomain near the injection imposing a zero pressure gradient and an adiabatic wall in a first investigation step, see Sect. 3. The cooling gas is helium, injected through a backward-facing step at a Mach number of 1.8 into the turbulent main flow of hot steam (gaseous  $\text{H}_2\text{O}$ ) at Mach-3.3.

The paper is organized as follows: In Sect. 2 the governing equations are provided and the numerical method is described. Section 3 shows the simulation setup, and the DNS results are shown in Sect. 4. Computational aspects of the DNS are discussed in Sect. 5. Finally, Sect. 6 summarizes the main findings and gives some concluding remarks.

## 2 Numerical Method

For the DNS we use our in-house high-order code NS3D, which has been successfully used for the calculation of film and effusion cooling in boundary-layer flow for non-reacting calorically perfect gases [11–14, 18]. The code is written in Fortran and parallelized using the MPI and OpenMP libraries. Detailed information about the fundamentals of NS3D can be found in, e.g., [1, 12, 13] and parallelization aspects are discussed in [5, 10, 11, 26].

### 2.1 Governing Equations

The governing equations for a gas-mixture flow of two non-reacting calorically perfect gases are the continuity equation, the three momentum equations, the energy equation, and the equation of state, all for the *mixture* values. Additionally, a sec-

ond continuity equation for one of the gas species has to be considered and the energy equation has to be modified to include the effects of ordinary and thermal diffusion, caused by concentration and temperature gradients, respectively. The non-dimensionalized equations in vector notation can be found in [14].

For the non-dimensionalization a reference length  $L^* = (\mu_\infty^* \cdot Re_\infty) / (\rho_\infty^* \cdot u_\infty^*)$  and the free-stream values of velocity, density, temperature, viscosity, and heat conductivity are used. Note that the pressure is made dimensionless by  $(\rho_\infty^* u_\infty^{*2})$ . The non-dimensional parameters are the Mach number  $Ma_\infty$ , the Prandtl number  $Pr$  and the Reynolds number  $Re_\infty$ . Dimensional quantities are marked by the asterisk \*, the subscript  $\infty$  refers to free-stream values. Throughout this paper, species 1 is the main flow gas and species 2 is the cooling gas. Both species have constant Prandtl number  $Pr_i$  and constant ratio of specific heats  $\kappa_i = c_{p,i}/c_{v,i}$ , where the species number is indicated by the subscript  $i$ . The mass fraction is denoted by  $c_i$ . Sutherland's law is used to calculate the dynamic viscosity  $\mu_i$  of the pure gases as a function of temperature and the mixing rule of Wilke [2] is then used to derive the mixture viscosity. For the diffusion coefficients  $D$  and  $D_T$ , see, e.g., [2].

## 2.2 Spatial Discretization and Time Integration

NS3D solves the governing equations in conservative formulation on a block-structured, curvilinear grid. High-order spatial accuracy is achieved by employing (alternatingly biased) compact finite differences of 6th-order. To enable a computationally parallel solution of the resulting equation system a sub-domain compact approach is used. Here, the sub-domains are decoupled by using explicit finite differences of 8th-order at overlapping grid points, thus breaking down the global tridiagonal equation system from the compact finite difference scheme to independent systems for each subdomain [11]. Time integration is performed by an explicit 4th-order 4-step Runge–Kutta scheme. To stabilize the simulation and to ensure de-aliasing, a 10th-order compact low-pass filter can be applied to the conservative variables at a chosen timestep interval [6]. Another effect of the filter is to strongly damp fluctuations in highly stretched grid regions, i.e. in buffer zones ahead of boundaries to minimize reflections. Additionally, sponge regions can be defined at boundaries to prevent undue reflections. If necessary, strong gradients due to shocks or at gas species interfaces can be treated by a shock-capturing procedure based on low-order filtering of the conservative variables [3]. A shock-sensor  $\sigma$  is applied based on the pressure and density gradients, and a 2nd-order filtering is locally performed. Then a blending is done between the original and the filtered flow field based on the value of the shock-sensor. The sensor, and therefore the influence of the low-order filter, is zero if the gradients are below a prescribed threshold.

**Table 1** Free-stream conditions for the DNS and thermophysical parameters of superheated steam and helium

Free stream			Steam	Helium
$Ma_\infty$	3.3	$Pr$	0.8	0.7
$U_\infty^*$	3383 (m/s)	$\kappa$	1.15	1.66
$T_\infty^*$	1980 (K)	$R^*$	461.5	2077.3 (J/(kgK))
$p_\infty^*$	0.28 (bar)	Sutherland $\mu_{ref}^*$	$1.12 \cdot 10^{-5}$	$1.85 \cdot 10^{-5}$ (kg/(ms))
$\rho_\infty^*$	0.0306 (kg/m <sup>3</sup> )	Sutherland $C^*$	1064.0	79.44 (K)
		Sutherland $T_{ref}^*$	350.0	273.1 (K)

### 3 Film-Cooling Setup

#### 3.1 Flow Configuration

In the experimental facility, a hydrogen-oxygen mixture is burnt in a detonation tube to provide rocket-engine-like stagnation conditions for a short testing time in the order of 7–10 ms. The burnt gas—superheated steam/gaseous H<sub>2</sub>O/GH<sub>2</sub>O—is expanded in an axisymmetric conical nozzle. For film-cooling experiments a cooling gas is injected tangentially to the nozzle wall through a backward facing step downstream of the throat. Only cases with supersonic cooling gas injection are investigated. Due to the short testing time, the nozzle walls virtually remain at their initial temperature. For more details on the experimental setup see [19]. The experimental flow has been analyzed using steady-state RANS of a one-species gas to yield the necessary free-stream conditions for the DNS of the film cooling in a near-wall domain, see [21]. The resulting free-stream parameters, here used for the inflow boundary, are listed in Table 1, along with the used thermophysical properties of hot GH<sub>2</sub>O and helium. In contrast to the experiment, where the nozzle wall is effectively strongly cooled due to the short-time experiment, all presented DNS use adiabatic wall conditions, and the free-stream pressure gradient is not considered.

#### 3.2 Film Cooling

The first step in the DNS is a validated turbulent simulation setup for the given flow conditions. Therefore the turbulent boundary-layer alone, i.e. flat-plate without coolant injection, has been simulated and compared to reference data, see [21]. A backward-facing step is now placed at a main-stream Reynolds number based on momentum thickness of  $Re_\theta \approx 1000$ , the boundary-layer thickness being  $\delta_{99}^* \approx 7.0$  mm. The step has a height of  $\delta_{step}^* = 1.2$  mm and the lower part contains the cooling-slot opening with a height of  $s^* = 0.7$  mm.

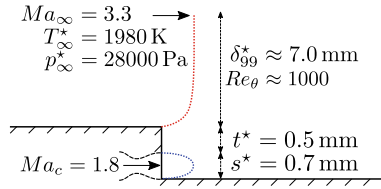


**Fig. 1** Detailed view of the geometry in the step region

**Table 2** Investigated blowing ratios and cooling stream condition

$F$	$p_c^*$ [Pa]	$p_c/p_\infty$	Cooling-channel exit condition
0.33	16350	0.584	Overexpanded
0.66	32700	1.168	Underexpanded
1.00	49050	1.752	Underexpanded

The setup is depicted in Fig. 1. Helium is used as cooling gas and injected through the slot opening. The channel flow is not simulated but a modelled approach is taken, where a parabolic velocity profile is prescribed at the slot opening according to a laminar flow in the cooling-gas channel. The centerline Mach number of the helium stream is fixed to  $Ma_c = 1.8$  and the temperature profile is then derived from the assumption of a total-temperature profile that varies linearly from the full value of  $T_{0,c}^* = 330$  K in the center to the recovery value at the walls; the subscript  $c$  denotes cooling gas values and the temperature on the centerline is about 200 K. The pressure  $p_c$  is taken constant over the slot height and the density  $\rho_c$  is derived from the equation of state. All coolant inlet values are kept constant due to the supersonic condition in the channel. Three blowing ratios,  $F = 0.33, 0.66, 1.00$  are investigated in this work, where  $F = (\rho^*u^*)_c / (\rho^*u^*)_\infty$ . The blowing ratio is varied by varying  $p_c$  (and thus  $\rho_c$  with  $\rho_c \propto p_c$  at constant  $T_c$ ), leading to different ratios of cooling gas to free-stream pressure  $p_c/p_\infty$ . The three cases are listed in Table 2. Note that the reported coolant inlet condition, i.e. the cooling-channel exit condition, is based on the free-stream pressure, not on the pressure behind the step without blowing.

### 3.3 Computational Setup, Initial Conditions, and Boundary Conditions

The full computational setup is depicted in Fig. 2. The length scales for the DNS are non-dimensionalized by the boundary-layer thickness  $\delta_{99,i}^*$  at the inlet. The origin of the coordinate system is placed at the upper edge of the backward-facing step, the regular domain extends from  $-80 \leq x/\delta_{99,i} \leq 87$  in the streamwise direction and has a height of  $y/\delta_{99,i} = 20$ . This corresponds to approximately eight boundary-

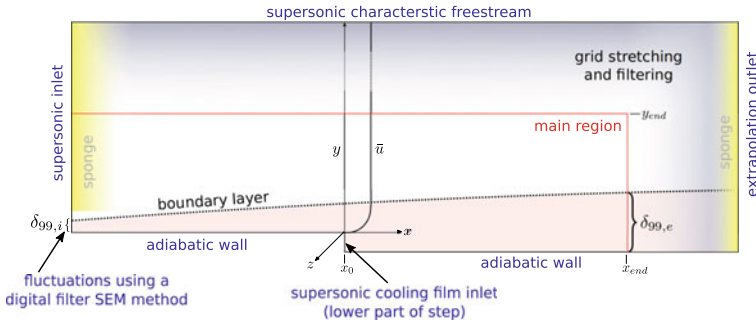


**Fig. 2** Setup for the film cooling DNS. The flow is assumed periodic in the  $z$ -direction

layer thicknesses at the injection location. In the spanwise direction the domain has a width of  $9\delta_{99,i}$  or approximately 3.7 boundary-layer thicknesses at the injection location. In both wall-normal and streamwise direction additional buffer regions with grid stretching and compact filtering are added to the regular domain to prevent numerical reflections at the boundaries. At the walls, the no-slip, no-penetration boundary conditions are imposed on the velocity components. The pressure and temperature are obtained by a 5th-order polynomial according to  $(\partial p/\partial y)_w = 0$  and  $(\partial T/\partial y)_w = 0$ , respectively; the density is calculated from the equation of state. At the free-stream boundary, a spatial supersonic characteristic condition is used where all flow variables are computed such that the gradient along spatial characteristics is zero, except for the pressure, which is computed from the equation of state [8]. At the outflow, all flow quantities are extrapolated from the field using a 2nd-order parabola. Additionally, a sponge region is defined ahead of the outflow boundary to help absorb fluctuations before they reach the outlet. At the supersonic main flow inlet, all values are fixed to the profile used as initial condition; additionally, unsteady artificial turbulent fluctuations using a digital filtering synthetic-eddy method (SEM) are superimposed within the boundary layer, see [15, 25]. Although a SEM-boundary provides a pseudo-turbulent flow field at the inlet of the domain, the flow needs about  $10\delta_{99,i}$  in streamwise direction to fully satisfy equilibrium turbulent-flow statistics. A sponge zone above the boundary layer in the inlet region prevents the far-field flow from being distorted by this transition process and also damps all shocks arising close to the inlet due to the supersonic condition.

## 4 Results

### 4.1 Main Flow Features and Cooling Effectiveness

For the three investigated cooling cases Figs. 3 and 4 show the time-averaged streamwise and wall-normal velocity, respectively. The flow field is averaged over a period of

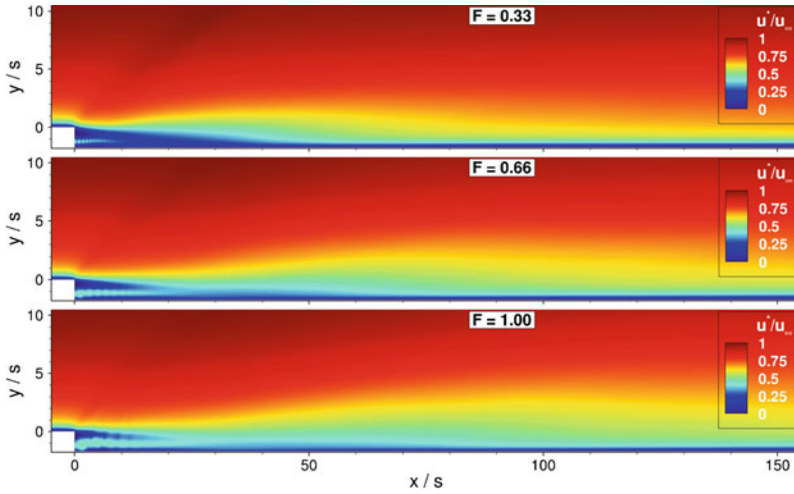


Fig. 3 Contours of streamwise velocity  $u$

at least  $u_{\infty}^* t_{avg}^*/s^* = 250$  and additionally spanwise averaged. (Note that averaging is only started after the initial transient phase has passed; additionally, the turbulent time scales in the cooling region are much smaller than in a regular flat-plate boundary-layer.) Due to the exit pressure of the coolant not being matched to the free stream, the existence of a nozzle shock-train is clearly visible in the velocities, with the wavelength of the shock-structures significantly increasing with higher blowing ratios. The higher cooling-gas pressure for the underexpanded cases ( $F = 0.66$  and  $F = 1.00$ ) also leads to a distinct upwards deflection of the hot oncoming stream. In the temperature plot in Fig. 5 the hot oncoming boundary layer is visible in the lower left, with the main-flow recovery temperature being  $T_{rec,\infty} = (1 + r \frac{\kappa-1}{2} Ma^2) \approx 1.76$ , where  $r = Pr^{1/3}$  is the turbulent recovery factor, and the total temperature of the helium being  $T_{0,c} \approx 0.17$ . The ratio of boundary-layer thickness to step-height is  $\delta_{99}/\delta_{step} \approx 6$ . Seban [23], Cary and Hefner [4], and Konopka et al. [17] investigated the influence of this ratio and found very little influence on the adiabatic cooling effectiveness. As can be expected, a higher blowing ratio leads to a longer sustaining cooling effect.

The adiabatic cooling effectiveness is defined as

$$\eta_{ad} = \frac{T_{rec,\infty} - T_w}{T_{rec,\infty} - T_{rec,c}}, \tag{1}$$

where  $T_{rec,c}$  is the coolant recovery temperature and  $T_w$  is the wall temperature with cooling. Figure 6 shows the distribution of  $\eta_{ad}$  along the cooled wall. All three blowing ratios show an initial region with perfect cooling ( $\eta_{ad} \approx 1$ ). Following Stollery [24] this is the “potential-core region” (where the mixing with the main-flow gas has not yet pierced through), which is terminated by the “film-breaking

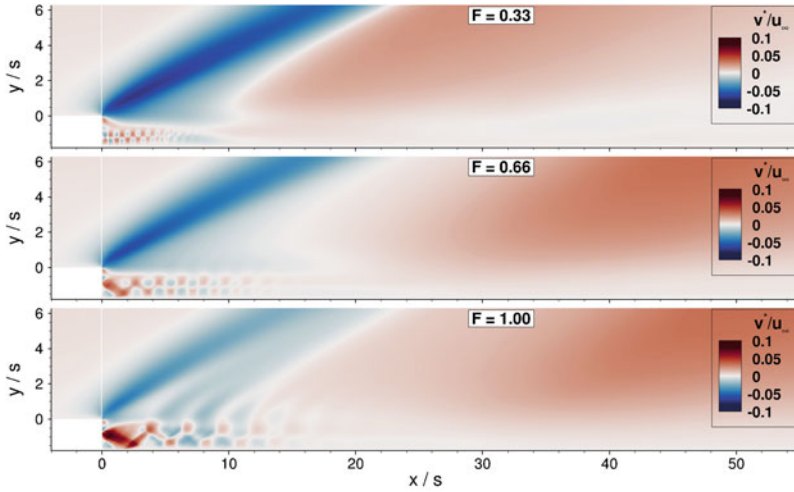


Fig. 4 Contours of wall-normal velocity  $v$ . Compared to Figs. 3 and 5, a smaller domain is shown

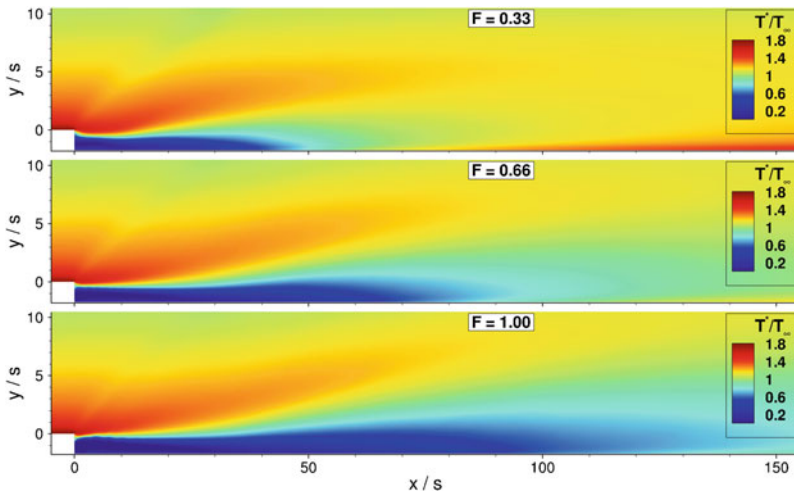


Fig. 5 Contours of temperature  $T$

point”. The following “boundary-layer region” shows a decay of the cooling effectiveness due to the transition of the laminar cooling-gas boundary layer to turbulence and the mixing with the hot gas. In this region, the cooling effectiveness can be approximated by

$$\eta = \left(\frac{x}{r}\right)^m, \tag{2}$$

**Table 3** Length  $r$  of potential-core region and exponent  $m$  in  $\eta = \left(\frac{x}{r}\right)^m$ 

$F$	$r/s$	$m$
0.33	26.55	-0.899
0.66	45.48	-0.741
1.00	57.34	-0.575

where  $r$  approximately describes the length of the potential-core region. This suggests that the obtained flow fields are self-similar in the respective boundary-layer region. The values for  $r$  and  $m$  for the three blowing ratios are listed in Table 3. This further highlights the better cooling performance of the higher blowing ratios; a higher cooling-gas injection rate leads to a thicker film that takes longer to be heated up by the main gas. The region with perfect cooling is increased and the following effectiveness decay is weaker, but both effects scale sub-linearly with the blowing ratio.

Another important quantity is the fluctuation of the wall temperature, as those fluctuations may cause problems with thermal fatigue. To that end, the fluctuation of the cooling effectiveness,

$$\eta'_{ad,rms} = \sqrt{\eta'_{ad}{}^2} = \frac{\sqrt{T_w'^2}}{T_{rec,\infty} - T_{rec,c}} = \frac{T'_{w,rms}}{T_{rec,\infty} - T_{rec,c}}, \quad (3)$$

is looked at, where the overbar denotes time-averaged data, the subscript *rms* refers to root-mean-square, and ' indicates a fluctuation. The distribution is also shown in Fig. 6. All cases show the same qualitative behavior: the fluctuation is close to zero in the potential-core region with perfect cooling, followed by a rise to a peak and a decay that approaches values on the order of those expected in supersonic turbulent flat-plate boundary-layers [27]. The two blowing ratios with  $p_c > p_\infty$  show a similar quantitative behavior. The rise starts somewhat earlier for  $F = 0.66$ , but similar peak values of  $\eta'_{ad,rms}$  are attained. In contrast, the lowest blowing rate with  $p_c < p_\infty$  shows a much higher peak value. The overexpansion of the coolant for  $F = 0.33$  leads to a shock train behind the slot with a much shorter wavelength than for the underexpanded cases, giving rise to short-wavelength disturbances (cf. Sect. 4.2).

For the prediction of the film-cooling effectiveness an often employed approach is the description of the mixing process using a boundary-layer model, in the attempt to scale different setups using a self-similarity correlation variable. A very common mixing-layer approach is by Goldstein [7], with the scaling variable

$$\xi = \frac{x^*}{F S^*} \frac{\rho^*}{\rho_\infty^*} \left( Re_c \frac{\mu_c^*}{\mu^*} \right)^{-0.25}, \quad (4)$$

where  $Re_c$  is the cooling-channel Reynolds number and  $\mu_c$  is the coolant viscosity, here both evaluated using averaged properties of the coolant. Values with the super-

**Fig. 6** Comparison of mean (solid lines) and fluctuating (rms) (dashed lines) cooling effectiveness. Dash-dotted lines show  $\eta = (\frac{x}{r})^m$ -approximation in boundary-layer region

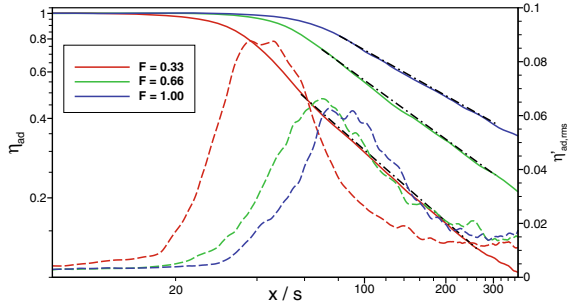
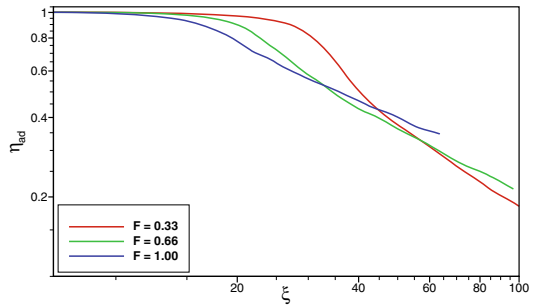


**Fig. 7** Scaling of cooling effectiveness



script \* are evaluated using the reference-temperature method. A correlation for the reference temperature of a non-air gas is given by Rasmussen [22]:

$$T^* = 0.566Pr^{1/3}T_\infty^* + (1 - 0.566Pr^{1/3})T_w^* + (0.566Pr^{5/6} - 0.421Pr) \frac{\kappa_1 - 1}{2} Ma_\infty^2 T_\infty^* \tag{5}$$

In the derivation of this formula a laminar, self-similar flat-plate boundary-layer with zero pressure gradient and constant wall temperature is assumed. The application of this formula in the present case is therefore questionable. (We note that it was applied in [19].) The reference temperature is calculated using the main-flow Prandtl number and the local (therefore varying) wall temperature for each case. The resulting correlation  $\eta(\xi)$  is shown in Fig. 7. As can be seen, no satisfying scaling collapse can be achieved. Neither the length of the potential-core region nor the slope of the effectiveness drop-off in the boundary-layer region collapse for the three blowing ratios. For a better match  $x$  must have an exponent depending on the blowing ratio in Eq. 4, which is so far effectively close to one. Note that for cooling in a laminar boundary-layer a scaling with  $\xi$  roughly proportional to  $x$  is successful [14].

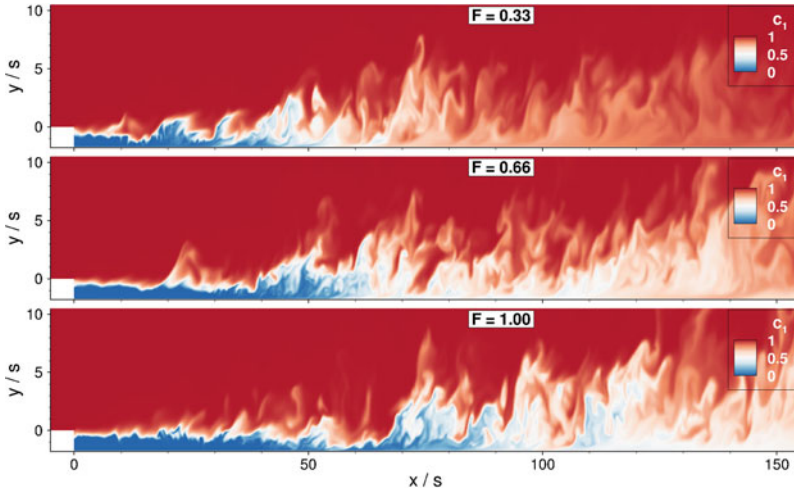


Fig. 8 Instantaneous snapshots of the main-gas mass fraction  $c_1$

### 4.2 Turbulent Mixing

The strong impact of the main-flow turbulence on the initially laminar cooling stream can be seen in Fig. 8, where snapshots of the main-gas mass fraction  $c_1$  are shown. Dynamical coherent structures (high-shear layers) known from laminar-turbulent boundary-layer transition scenarios quickly appear in the mixing layer, indicating a quick transition of the mixing shear-layer and break-up of the coolant stream.

The structures appear the farther downstream the larger the blowing ratio is. The higher-density and thus higher-momentum jets seem more resistant to distortion through the vortices present in the main-flow boundary-layer. Further evidence is provided by the turbulent kinetic energy (TKE)

$$k = \frac{1}{2\bar{\rho}} \cdot (\overline{\rho u''u''} + \overline{\rho v''v''} + \overline{\rho w''w''}), \tag{6}$$

where  $''$  indicates a Favre-fluctuation. The time- and spanwise-averaged contours of  $k$  are shown in Fig. 9. High TKE values also indicate intense mixing due to turbulence. With an increase of the blowing ratio and overpressure the TKE in the mixing zone decreases and the mixing zones lift up, meaning less coolant is transported away from the wall. Generally, the turbulent kinetic energy levels in the mixing region are higher than in the oncoming boundary layer. Additionally, Fig. 9 shows wall-normal profiles of the streamwise velocity at downstream locations  $x/s = 10$ ,  $x/s = 30$ ,  $x/s = 80$ . Pink dots in the profiles mark locations of generalized inflection points (GIPs), determined from  $\frac{\partial}{\partial y} \left( \rho \frac{\partial u}{\partial y} \right) = 0$  [20]. The existence of GIPs in the averaged

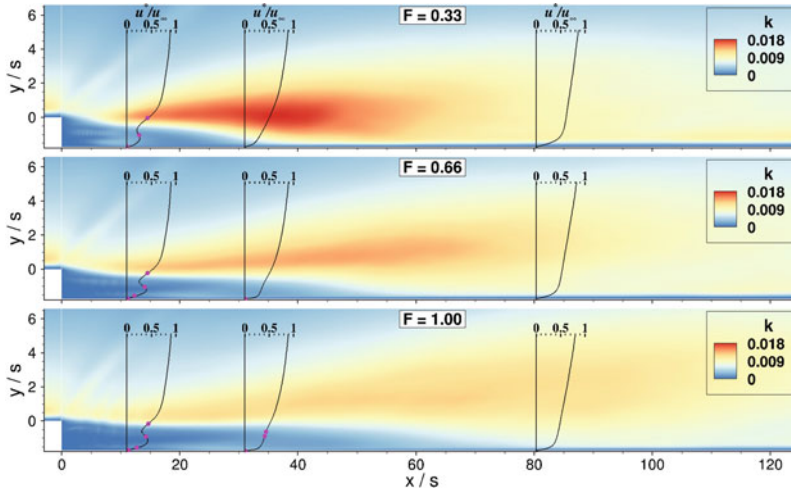


**Fig. 9** Contours of turbulent kinetic energy  $k$ . The lines show wall-normal profiles of the velocity component  $u$  at  $x/s = 10, x/s = 30, x/s = 80$ , pink dots mark generalized inflection points

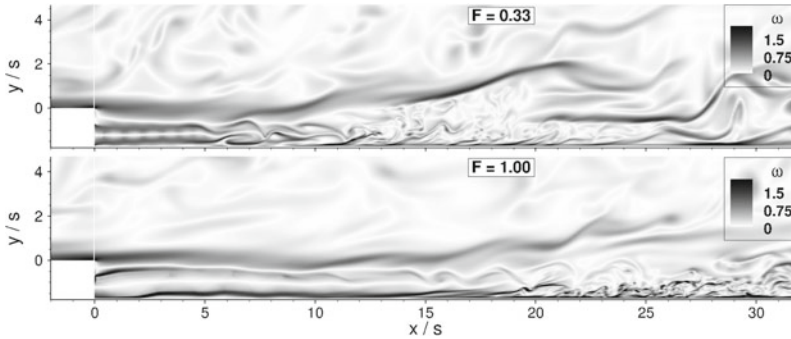


**Fig. 10** Instantaneous snapshots of the absolute vorticity  $\omega$

velocity profile leads to the existence of an inviscid instability in the mean flow, feeding the generation of turbulence in the mixing zone.

Figure 10 shows details of the flow field in the mixing region by instantaneous total-vorticity contours. Three different disturbance scales can be identified: main gas turbulence (MGT, for  $y/s > 0$  and  $x/s$  small), cooling gas turbulence (CGT, for  $F = 1.00$  and  $x/s > 20$ ), and the shock-train structures near the injection (CGS, for  $F = 0.33$  and  $0 \leq x/s \leq 5$ ). The CGT scales are much smaller than the MGT scales due to the higher density ( $l \propto l^+ \cdot \rho^{-\frac{1}{2}}$ ), and thus the direct infection of the laminar cooling stream by the MGT is impeded with higher  $F$ . Additionally, the CGS spatial wavenumber gets smaller. For  $F = 0.33$  the CGT seems clearly triggered by an instability of the CGS due to its wavenumber scale matching the CGT scale.

## 5 Computational Aspects

The simulations for the presented film-cooling DNS are carried out on the Cray XC40 ‘Hazelhen’ supercomputer at the federal high performance computing center Stuttgart (HLRS). Additional simulations, especially for the validation of the turbulent baseflow (see [21]), have been run on the NEC SX-ACE ‘Kabuki’ vector computer system at HLRS.

The simulation code NS3D is parallelized using a hybrid MPI/OpenMP approach. For the version used in this investigation, the computational grid can be split in the  $x$ - and  $y$ -direction using MPI for inter-domain communication and within a domain the  $z$ -direction is parallelized using the shared-memory OpenMP library. Recently, scaling aspects of this approach have been investigated and some shortcomings have been found [5]. The number of cores used for the  $z$ -direction is limited to the 24 available cores per node (then with one MPI process per node), independent of the number of grid points. Additionally, the code has been found to scale well up to 12 OpenMP threads with the parallel efficiency dropping to only around 55% for 24 threads due to socket-remote memory access in the ccNUMA architecture of the Cray XC40. This has been taken as incentive to invest time into improving the code performance and scalability to very high core counts by implementing a full MPI decomposition in all spatial directions. Figure 11 shows the speed-up and efficiency as a function of the CPUs used for the parallelization of the  $z$ -direction for the old code version (pure increase of OpenMP-threads) and the improved variant (mixed MPI decomposition and increase of OpenMP-threads). The test case consists of  $6912 \times 600 \times 256$  grid points in the  $x$ -,  $y$ -, and  $z$ -direction, respectively. For the baseline case the domain is split into 768 MPI sub-domains in the  $x - y$ -plane using one CPU per MPI process. The scaling is then done using parallelization of the  $z$ -direction up to 24 CPUs, giving a scaling from 768 to 18432 CPUs total. Very good results have been achieved showing a large increase in efficiency for high core numbers and thus enabling even higher parallelization while keeping the already-good base performance of the code, see [26]. The scaling using parallelization of the  $z$ -direction is now on par with scaling (by pure domain decomposition) in the  $x$ - $y$  plane, see [11].

These improvements were implemented in a from-ground revised version of the code, which was done for the single-species version of NS3D first. The computational work for the present results was started before the extension to two-component flows was implemented and thus the “old” NS3D was used. Further work for this project will be using the revised code version. The computational details of the presented film-cooling DNS are listed in Table 4. The grid is highly decomposed in the  $x$ - and  $y$ -direction with only  $35 \times 35$  grid points per domain, while the  $z$ -direction consists of 1024 grid points (due to the limitations mentioned above).

**Performance optimization workshop** The HLRS biannually hosts the “Optimization of Scaling and Node-level Performance” workshop, where code developers jointly work with the cluster experts of the supercomputing center on their simulation software. The knowledge gained during these workshop has greatly helped

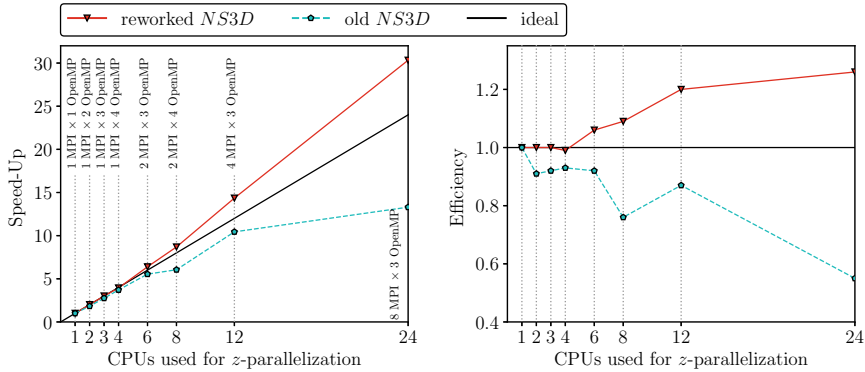


**Fig. 11** (Left) Speed-up and (right) efficiency for a variation of the number of CPUs used for the z-parallelization. Scaling is done using pure OpenMP for the old NS3D and a mixture of MPI/OpenMP for the reworked code

**Table 4** Computational details of the investigated film-cooling DNS

Parameter	Value
MPI ranks $\times$ OpenMP threads = total CPUs	$1248 \times 12 = 14976$
Grid points of the main domain $N_x \times N_y \times N_z$	$4130 \times 315 \times 1024$
Grid points of the step domain $N_x \times N_y \times N_z$	$2170 \times 105 \times 1024$
Grid points per MPI rank $N_x \times N_y \times N_z$	$35 \times 35 \times 1024 = 1\,254\,400$
Total grid points	$1.57 \times 10^9$
Computed time steps	300000

in the performance optimization of the revised NS3D code and its scaling aspects. Due to the time investment from both the people working on NS3D and the team of HLRS, see the acknowledgments, the code is well suited for current and next-generation HPC systems at HLRS.

## 6 Conclusions and Outlook

High-order DNS of a supersonic film-cooling configuration have been performed for various blowing ratios  $F = (\rho^* u^*)_c / (\rho^* u^*)_\infty$ . Analysis of the adiabatic cooling effectiveness  $\eta_{ad}$  shows the expected better performance for higher blowing ratios. Here the laminar-cooling-gas density and pressure have been varied at kept temperature and Mach number. A high momentum by high density and pressure of the cooling stream makes it less vulnerable to turbulence infection and mixing, whereas blowing with an overexpanded cooling gas does the opposite. The results for  $\eta$  have been scaled using the common Goldstein formula, but no satisfying results could be

achieved. The correlation formula does not include the turbulent mixing that depends strongly on the flow structure; the evaluation of the needed reference  $T^*$  is non-trivial by the mixing process. The DNS show that the turbulent-kinetic-energy maximum reduces with increasing  $F$ , thus the mixing is decreased and  $\eta$  does not decay as fast. A next step is the investigation of the slot height and the coolant Mach number.

**Acknowledgements** Financial support has been provided by the German Research Foundation (Deutsche Forschungsgemeinschaft—DFG) in the framework of the Sonderforschungsbereich Transregio 40 (SFB-TRR40, SP A4). The simulations were performed on the national supercomputers Cray XC40 ‘Hazelhen’ and NEC SX-ACE ‘Kabuki’ at the High Performance Computing Center Stuttgart (HLRS) under grant GCS\_Lamt, ID 44026. The authors and the people working on NS3D at IAG in the groups on “Transition and Turbulence” and “Boundary-Layer Flows” would like to thank the team of the HLRS, especially Björn Dick, Stefan Andersson (Cray), and Holger Berger (NEC), for their continued support in developing software for HPC applications.

## References

1. A. Babucke, Direct numerical simulation of noise-generation mechanisms in the mixing layer of a jet. Ph.D. thesis, Universität Stuttgart (2009)
2. R.B. Bird, W.E. Stewart, E.N. Lightfoot, *Transport Phenomena* (John Wiley & Sons Inc., 1960)
3. C. Bogey, N. de Cacqueray, C. Bailly, A shock-capturing methodology based on adaptative spatial filtering for high-order non-linear computations. *J. Comput. Phys.* **228**(5), 1447–1465 (2009). <https://doi.org/10.1016/j.jcp.2008.10.042>
4. A.M. Cary, J.N. Hefner, Film-cooling effectiveness and skin friction in hypersonic turbulent flow. *AIAA J.* **10**(9), 1188–1193 (1972). <https://doi.org/10.2514/3.50348>
5. P.C. Dörr, Z. Guo, J.M.F. Peter, M.J. Kloker, Control of traveling crossflow vortices using plasma actuators, in *High Performance Computing in Science and Engineering '17*, ed. by W.E. Nagel, D.B. Kröner, M.M. Resch (Springer International Publishing, 2017). [https://doi.org/10.1007/978-3-319-68394-2\\_15](https://doi.org/10.1007/978-3-319-68394-2_15)
6. D.V. Gaitonde, M.R. Visbal, Padé-type higher-order boundary filters for the Navier-Stokes equations. *AIAA J.* **38**(11), 2103–2112 (2000). <https://doi.org/10.2514/2.872>
7. R.J. Goldstein, Film cooling. *Adv. Heat Transf.* **7**, 321–379 (1971). [https://doi.org/10.1016/S0065-2717\(08\)70020-0](https://doi.org/10.1016/S0065-2717(08)70020-0)
8. P.J. Harris, HF Fasel, Numerical investigation of unsteady plane wakes at supersonic speeds, in *34th Aerospace Sciences Meeting and Exhibit* (1996). <https://doi.org/10.2514/6.1996-686>. aIAA-1996-686
9. K.A. Juhany, M.L. Hunt, Flowfield measurements in supersonic film cooling including the effect of shock-wave interaction. *AIAA J.* **32**(3), 578–585 (1994). <https://doi.org/10.2514/3.12024>
10. M. Keller, M.J. Kloker, Direct numerical simulations of film cooling in a supersonic boundary-layer flow on massively-parallel supercomputers, in *Sustained Simulation Performance* (Springer International Publishing, 2013), pp 107–128. [https://doi.org/10.1007/978-3-319-01439-5\\_8](https://doi.org/10.1007/978-3-319-01439-5_8). Or see ResearchGate.net
11. M. Keller, M.J. Kloker, DNS of effusion cooling in a supersonic boundary-layer flow: influence of turbulence, in *44th AIAA Thermophysics Conference* (2013). <https://doi.org/10.2514/6.2013-2897>. aIAA-2013-2897
12. M. Keller, M.J. Kloker, Effusion cooling and flow tripping and in laminar and supersonic boundary-layer and flow. *AIAA J.* **53**(4) (2015). <https://doi.org/10.2514/1.J053251>
13. M. Keller, M.J. Kloker, Direct numerical simulation of foreign-gas film cooling in supersonic boundary-layer flow. *AIAA J.* **55**(1), 99–111 (2016). <https://doi.org/10.2514/1.J055115>

14. M. Keller, M.J. Kloker, H. Olivier, Influence of cooling-gas properties on film-cooling effectiveness in supersonic flow. *J. Spacecr. Rocket.* **52**(5), 1443–1455 (2015). <https://doi.org/10.2514/1.A33203>
15. M. Klein, A. Sadiki, J. Janicka, A digital filter based generation of inflow data for spatially developing direct numerical or large eddy simulations. *J. Comput. Phys.* **186**(2), 652–665 (2003). [https://doi.org/10.1016/s0021-9991\(03\)00090-1](https://doi.org/10.1016/s0021-9991(03)00090-1)
16. M. Konopka, M. Meinke, W. Schröder, Large-eddy simulation of supersonic film cooling at finite pressure gradients, in *High Performance Computing in Science and Engineering* (Springer International Publishing, 2011), pp. 353–369. [https://doi.org/10.1007/978-3-642-23869-7\\_26](https://doi.org/10.1007/978-3-642-23869-7_26)
17. M. Konopka, M. Meinke, W. Schröder, Large-eddy simulation of shock/cooling-film interaction. *AIAA J.* **50**(10), 2102–2114 (2012). <https://doi.org/10.2514/1.J051405>
18. J. Linn, M.J. Kloker, Effects of wall-temperature conditions on effusion cooling in a supersonic boundary layer. *AIAA J.* **49**(2), 299–307 (2011). <https://doi.org/10.2514/1.J050383>
19. S. Ludescher, H. Olivier, Experimental investigations of film cooling in a conical nozzle under rocket-engine-like flow conditions. *AIAA J.* **57**(3), 1172–1183 (2018). <https://doi.org/10.2514/1.j057486>
20. L.M. Mack, Boundary-layer linear stability theory, in *Special Course on Stability and Transition of Laminar Flow - AGARD-R-709*, AGARD (1984)
21. J.M.F. Peter, M.J. Kloker, Preliminary work for DNS of rocket-nozzle film-cooling, in *Deutscher Luft- und Raumfahrtkongress DLRK, DLRK-2017-450178* (2017), <http://d-nb.info/1142014584>. Or see ResearchGate.net
22. M.L. Rasmussen, *Hypersonic Flow* (Wiley, New York, 1994)
23. R.A. Seban, Effects of initial boundary-layer thickness on a tangential injection system. *J. Heat Transf.* **82**(4), 392–393 (1960). <https://doi.org/10.1115/1.3679966>
24. J.L. Stollery, A.A.M. El-Ehwany, A note on the use of a boundary-layer model for correlating film-cooling data. *Int. J. Heat Mass Transf.* **8**(1), 55–65 (1965). [https://doi.org/10.1016/0017-9310\(65\)90097-9](https://doi.org/10.1016/0017-9310(65)90097-9)
25. E. Touber, Unsteadiness in shock-wave/boundary-layer interactions. Ph.D. thesis, University of Southampton (2010)
26. C. Wenzel, J.M.F. Peter, B. Selent, M.B. Weinschenk, U. Rist, M.J. Kloker, DNS of compressible turbulent boundary layers with adverse pressure gradients, in *High Performance Computing in Science and Engineering '17*, ed. by W.E. Nagel, D.B. Kröner, M.M. Resch (Springer International Publishing, 2018). <https://doi.org/10.1007/978-3-030-13325-2>
27. C. Wenzel, B. Selent, M.J. Kloker, U. Rist, DNS of compressible turbulent boundary layers and assessment of data-/scaling-law quality. *J. Fluid Mech.* **842**, 428–468 (2018). <https://doi.org/10.1017/jfm.2018.179>